

Probing the C_{60} triplet state coupling to nuclear spins inside and out

Vasileia Filidou, Salvatore Mamone, Stephanie Simmons, Steven D. Karlen, Harry L. Anderson, Christopher W. M. Kay, Alessandro Bagno, Federico Rastrelli, Yasujiro Murata, Koichi Komatsu, Xuegong Lei, Yongjun Li, Nicholas J. Turro, Malcolm H. Levitt and John J. L. Morton

Phil. Trans. R. Soc. A 2013 **371**, 20120475, published 5 August 2013

References

This article cites 48 articles, 4 of which can be accessed free
<http://rsta.royalsocietypublishing.org/content/371/1998/20120475.full.html#ref-list-1>

Subject collections

Articles on similar topics can be found in the following collections

[quantum physics](#) (83 articles)

Email alerting service

Receive free email alerts when new articles cite this article - sign up in the box at the top right-hand corner of the article or click [here](#)

rsta.royalsocietypublishing.org



Research

Cite this article: Filidou V, Mamone S, Simmons S, Karlen SD, Anderson HL, Kay CWM, Bagno A, Rastrelli F, Murata Y, Komatsu K, Lei X, Li Y, Turro NJ, Levitt MH, Morton JLL. 2013 Probing the C_{60} triplet state coupling to nuclear spins inside and out. *Phil Trans R Soc A* 371: 20120475.
<http://dx.doi.org/10.1098/rsta.2012.0475>

One contribution of 13 to a Theo Murphy Meeting Issue 'Nanolaboratories: physics and chemistry of small-molecule endofullerenes'.

Subject Areas:

quantum physics

Keywords:

electron paramagnetic resonance, triplet state, nuclear spin, endofullerenes, *ortho–para* interconversion

Author for correspondence:

Vasileia Filidou
e-mail: v.filidou@ucl.ac.uk

[†] Deceased 24 November 2012.

Probing the C_{60} triplet state coupling to nuclear spins inside and out

Vasileia Filidou^{1,2}, Salvatore Mamone³, Stephanie Simmons^{1,2}, Steven D. Karlen⁴, Harry L. Anderson⁴, Christopher W. M. Kay^{1,5}, Alessandro Bagno⁶, Federico Rastrelli⁶, Yasujiro Murata⁷, Koichi Komatsu⁷, Xuegong Lei⁸, Yongjun Li⁸, Nicholas J. Turro^{8,†}, Malcolm H. Levitt³ and John J. L. Morton^{1,9}

¹London Centre for Nanotechnology, University College London, London WC1H 0AH, UK

²Department of Materials, University of Oxford, Parks Road, Oxford OX1 3PH, UK

³School of Chemistry, University of Southampton, Southampton SO17 1BJ, UK

⁴Department of Chemistry, University of Oxford, Oxford OX1 3TA, UK

⁵Institute of Structural and Molecular Biology, University College London, Gower Street, London WC1E 6BT, UK

⁶Dipartimento di Scienze Chimiche, Università di Padova, via Marzolo 1, 35131 Padova, Italy

⁷Institute for Chemical Research, Kyoto University, Uji, Kyoto 611-0011, Japan

⁸Department of Chemistry, Columbia University, New York, NY 10027, USA

⁹Department of Electronic and Electrical Engineering, University College London, London WC1E 7JE, UK

The photoexcitation of functionalized fullerenes to their paramagnetic triplet electronic state can be studied by pulsed electron paramagnetic resonance (EPR) spectroscopy, whereas the interactions of this state with the surrounding nuclear spins can be observed by a related technique: electron nuclear double resonance (ENDOR). In this study, we present EPR and ENDOR studies on a functionalized exohedral fullerene system, dimethyl[9-hydro (C₆₀-Ih)[5,6]fulleren-1(9H)-yl]phosphonate (DMHFP),

where the triplet electron spin has been used to hyperpolarize, couple and measure two nuclear spins. We go on to discuss the extension of these methods to study a new class of endohedral fullerenes filled with small molecules, such as $\text{H}_2@C_{60}$, and we relate the results to density functional calculations.

1. Introduction

The photo-generated triplet state of organic chromophores has been extensively studied through pulsed electron paramagnetic resonance (EPR), time-resolved EPR (TR-EPR), time-resolved electron nuclear double resonance (TR-ENDOR) and optically detected magnetic resonance spectroscopy [1–4]. These techniques shed light on the photophysical properties of triplet states, their interactions, the exciton delocalization and the triplet exciton transfer [5]. The first EPR experiment on photoexcited triplet states was conducted by Hutchison *et al.* [6], who measured the lifetime of the triplet state of naphthalene in a durene single-crystal host. Since then, many studies have been performed on molecular systems in their triplet state, motivated by applications in chemistry, biology and medicine, such as improving our understanding of photosynthesis, the binding of aromatic ligands to DNA and photodynamic therapy [7–11].

An important characteristic of certain triplet states that can be exploited for quantum information processing and dynamic nuclear polarization applications is the high yield of formation as well as the creation of large spin polarization. This triplet spin polarization can be transferred to nearby, coupled nuclear spins through continuous wave (CW) microwave illumination [12,13], via the dynamic nuclear polarization family of methods or by the application of microwave pulses [14]. Even if the triplet state is not highly polarized upon formation, other properties such as a substantial difference in the decay rates of the triplet sublevels to the ground state can lead to spin polarization that can subsequently be transferred to a nuclear spin [15]. The transient triplet electron spin has been proposed as a mediator to indirectly couple two nuclear spins, for example in a homonuclear fullerene system [16]. In this scheme, the feasibility of high-power nuclear entangling gates depends critically on a combination of factors, including the triplet lifetime and the strength of the hyperfine interaction between the triplet and the nuclear spins. A related proposal, based on a heteronuclear system and exploiting the spinor nature of the triplet state, was experimentally applied to the fullerene dimethyl[9-hydro(C60-Ih)]5,6]fulleren-1(9*H*)-yl]phosphonate (DMHFP) molecule (figure 1*a*). In that work, ultrafast nuclear entangling gates were implemented on a time scale of hundreds of nanoseconds [17].

In §2, we give a brief background of the underlying physical mechanisms that give birth to the triplet state in fullerenes and we present detailed EPR studies at 10 GHz (X-band) and 34 GHz (Q-band) for the characterization of the DMHFP triplet state. In the second part of this work, we describe photoexcited EPR and ENDOR experiments performed on the $\text{H}_2@C_{60}$ molecule (figure 1*b*), relating the results to density functional theory (DFT) calculations.

2. The triplet-level system

In C_{60} , the triplet state is typically created through the first excited singlet state via a mechanism called intersystem crossing (ISC), which originates from the spin–orbit coupling. In general, ISC rates vary from 10^4 to 10^{12} s^{-1} , and are approximately 10^{10} s^{-1} for the fullerene C_{60} . This process populates (unevenly, in general) the levels of the lowest triplet state, which are split by a zero field splitting (ZFS; figure 1*c*). Upon the application of a static magnetic field, the zero-field triplet levels mix in an orientation-dependent manner, resulting in the T_0 , T_- and T_+ electron spin states. These states may further split owing to hyperfine couplings between the triplet and any nearby nuclear spins. The triplet state decays to the ground singlet state directly, whereas spin lattice relaxation between the triplet sublevels can also be present especially at elevated temperatures.

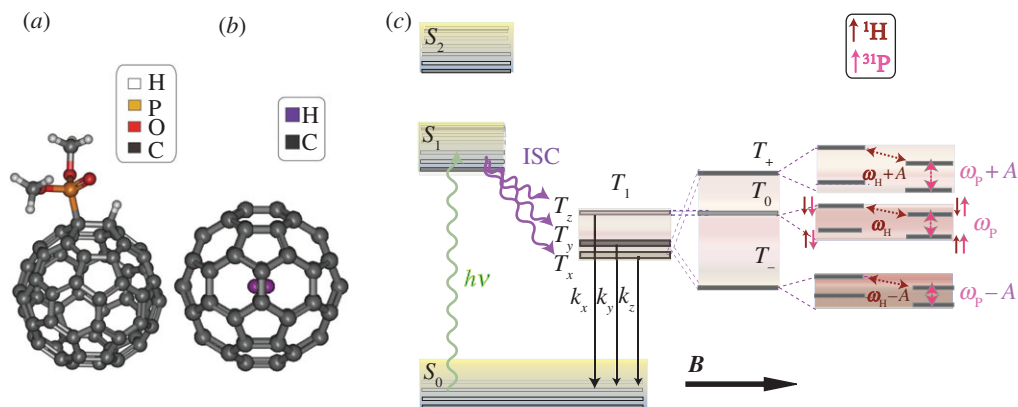


Figure 1. (a) The DMHFP molecule. The two nuclear spins ¹H and ³¹P are marked with white and yellow, respectively. (b) The H₂@C₆₀ molecule. An H₂ molecule lies in the centre of the fullerene cage and is coloured in purple. (c) Representation of the energy-level diagram of the DMHFP. Upon photoexcitation to the first singlet state, ISC (unequally) populates the triplet sublevels T_x, T_y, T_z. The application of a magnetic field creates the T₊, T₀ and T₋ levels, which are orientation-dependent linear combinations of the zero field sublevels T_x, T_y, T_z. These levels couple to the two nuclear spins, ¹H, ³¹P, causing further splittings owing to nuclear Zeeman and hyperfine interactions. The two nuclear spins are marked with red and pink arrows. ω_{H,P} is the Larmor frequency of each nuclear spin and A is the hyperfine interaction. (Online version in colour.)

We use EPR spectroscopy to characterize the systems under investigation and determine all the interactions involved by extracting the terms of the spin Hamiltonian

$$\hat{H} = \mu_B \mathbf{S} \mathbf{g}_e \mathbf{B} + \mathbf{S} \mathbf{D} \mathbf{S} + \sum_{i=1} \mathbf{S} \mathbf{A}(i) \mathbf{I}_i + J I_{1,z} I_{2,z} + \gamma_{i,n} \mathbf{I}_i \cdot \mathbf{B}, \quad (2.1)$$

where \mathbf{B} is the applied magnetic field, \mathbf{g}_e is the electron \mathbf{g}_e -factor tensor, μ_B is the Bohr magneton and \mathbf{D} is the ZFS tensor for the $S = 1$ triplet state. In the principal axis system, the ZFS term of the Hamiltonian $\mathbf{S} \mathbf{D} \mathbf{S}$ can be written alternatively as $D(S_z^2 - S(S+1)^2/3) + E(S_x^2 - S_y^2)$ with $D = 3D_z/2$ and $E = (D_x - D_y)/2$. $\mathbf{A}(i)$ is the hyperfine coupling tensor between the triplet and the nuclear spins i , J is the coupling between the nuclear spins and $I_{i,z}$ is the projection of \mathbf{I}_i along z which is defined by B_0 .

3. DMHFP

We synthesized the exohedral fullerene derivative DMHFP with two nuclear spins directly bonded to the cage (a proton, ¹H, and a phosphorus, ³¹P), according to the procedure reported in [18]. The sample of 4×10^{-4} M concentration in d₈-toluene was deoxygenated using five freeze–pump–thaw cycles, flame sealed under vacuum and flash frozen in liquid nitrogen.

TR-EPR experiments of the photoexcited paramagnetic state of DMHFP were performed at 34 GHz (Q-band) on a Bruker Elexys 580 e spectrometer equipped with a low-temperature helium flow cryostat. Photoexcitation was performed using an optical parametric oscillator pumped by a Nd–YAG laser of variable repetition rate, with a pulse width of 7 ns and 10 mJ energy per pulse.

The contour plot shown in figure 2 illustrates the decay of the TR-EPR signal following the laser pulse, and a single spectrum is shown for reference in figure 3a. The EPR spectrum is broadened by the ZFS term (\mathbf{D}), which causes the EPR transition frequencies to vary according to the orientation of the molecule with respect to the applied static magnetic field [2,19]. Therefore, each magnetic field position in the EPR spectrum corresponds to molecules with different orientations, and the four distinct peaks (named here as pairs: ‘inner’ and ‘outer’ peaks) reflect molecules with one of their three principal axes (x , y or z) parallel to the magnetic field. For example, the field positions marked with Z⁺ and Z⁻ in the spectrum refer to molecules with

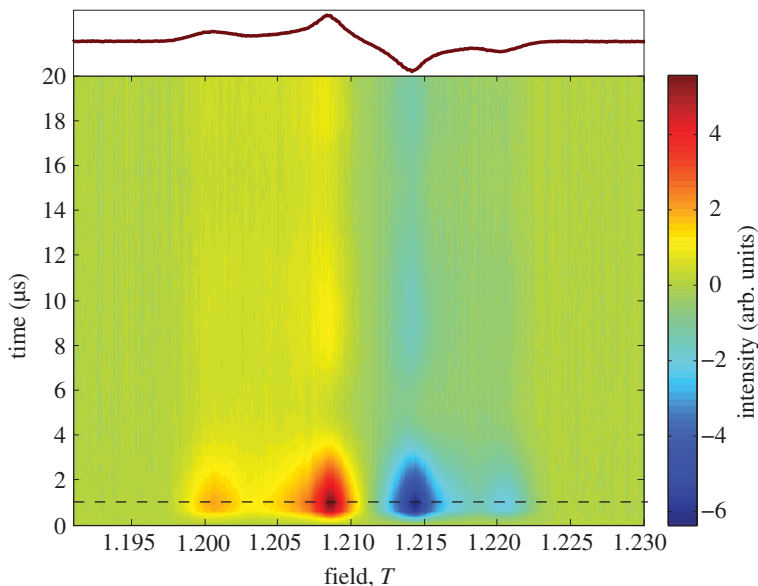


Figure 2. Three-dimensional plot of the TR-EPR field sweep spectra at 50 K at Q-band of the DMHFP. The build-up and the decay of the (CW) EPR signal is monitored as the delay after the pulse is increased up to 20 μs . The build-up time of about 1 μs until the spectrum reaches maximum intensity is the response of the spectrometer. The microwave power is 0.5 mW. (Online version in colour.)

their z -axes parallel to the magnetic field, and the superscripts refer to resonances situated at high and low magnetic fields, respectively. The molecular orientation selection achieved at all other field positions is not completely pure, as other non-canonical orientations also contribute to the signal intensity.

The EPR spectrum has an AAEE pattern (A, absorption; E, emission) and is symmetric in high and low fields. In general, a triplet EPR spectrum is a combination of an absorption and an emission component between pairs of levels with $\Delta M_s = \pm 1$, as shown in figure 3*b*, and is not to be confused with the derivative line shape of an absorption spectrum seen in conventional field-modulated CW EPR methods. In figure 3*c*, we show for comparison the simulated spectrum assuming that the three triplet levels are thermally populated (as opposed to hyperpolarized), yielding a characteristic Pake pattern.

In order to extract the terms of the Hamiltonian and determine the polarization of the triplet state, we perform simulations of the Q-band TR-EPR spectrum using Easyspin [20] (figure 3*a*). From the fit, we extract the principal values of the g -tensor, $g_{xx} = 2.00076$, $g_{yy} = 2.00224$, $g_{zz} = 2.00274$ with an anisotropy of $g_{zz} - g_{xx} = 0.0019$. The effect of this g -anisotropy in the spectrum would be more pronounced at even higher frequencies than the 34 GHz used here. The ZFS D is given by half the separation between the edges of the spectrum (marked with Z) and the central splitting in the spectrum provides an indication of the ZFS anisotropy.

The negative sign of the ZFS parameter from the fit $D = -317$ MHz is consistent with the negative D value of the fullerene C_{60} , and the large E anisotropy of -53 MHz reveals a significant deviation from axial symmetry. The population ratio, $|p_x - p_z|/|p_y - p_z| = 0.32$, indicates that the ISC populates mostly the T_y sublevel, considering that a negative D leads to a polarization pattern of $|p_x, p_y| > p_z$. Previous studies at X-band reveal the same population ratio and a similar D -tensor [17].

Studies of the time evolution of the triplet signal were also performed using X-band EPR (9.7 GHz). We apply soft (selective) microwave pulses of 64 and 128 ns duration for the $\pi/2$ and the π pulses, respectively, and we extract series of electron spin echo-detected field sweep (ESE-FS) spectra in which the delay after the laser flash was varied up to 750 μs (figure 4). The

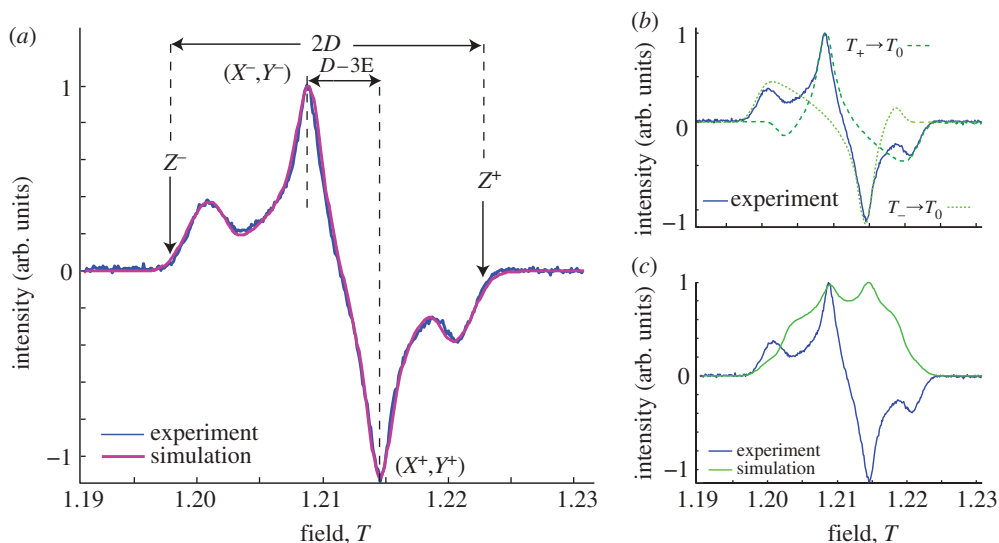


Figure 3. (a) TR-EPR spectrum of DMHFP and fitting. We observe four peaks with the polarization pattern AAEE (A, absorption; E, emission). The total width of the spectrum is twice the zero field splitting ($2D$) and the separation of the two inner peaks, which is $D - 3E$, is a measure of the anisotropy. (b) The polarization pattern of the spectrum reflects the two contributions between the triplet sublevels, the emission from T_+ to T_0 and the absorption from T_- to T_0 . (c) Simulated spectrum assuming the triplet populations are in thermal equilibrium. (Online version in colour.)

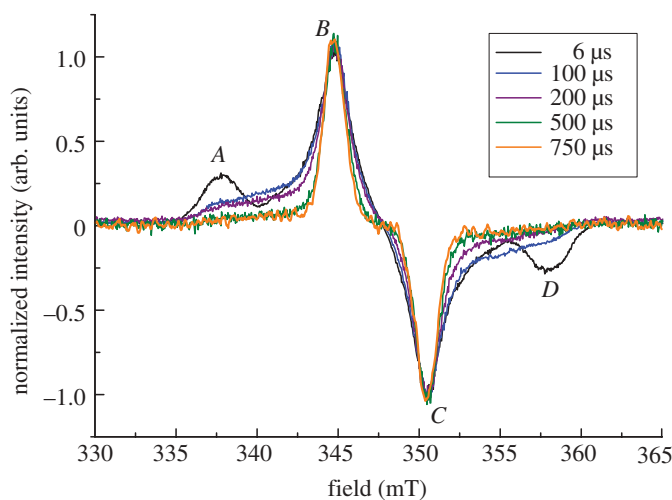


Figure 4. Normalized electron spin echo of DMHFP as a function of magnetic field, measured at different delays after the laser flash (X-band, 5 K). The outer peaks decay more quickly than the inner peaks and by $750 \mu\text{s}$ have completely decayed. The labels *A*, *B*, *C*, *D* marked on the spectrum refer to points at which ENDOR spectra were taken. (Online version in colour.)

quick decay of the outer peaks compared with the inner peaks indicates the presence of an anisotropic relaxation mechanism. The preservation of the symmetric shape of the spectra within this range shows that no substantial triplet relaxation between the triplet sublevels occurs. By performing an inversion recovery experiment at the field position 'B' (with respect to figure 4), we are able to extract the electron spin triplet T_1 relaxation time by monitoring the decay of the echo after flipping the initial magnetization with an additional π pulse. From the fitting of this curve, it can be inferred that the T_1 is longer than any of the observed triplet recombination times,

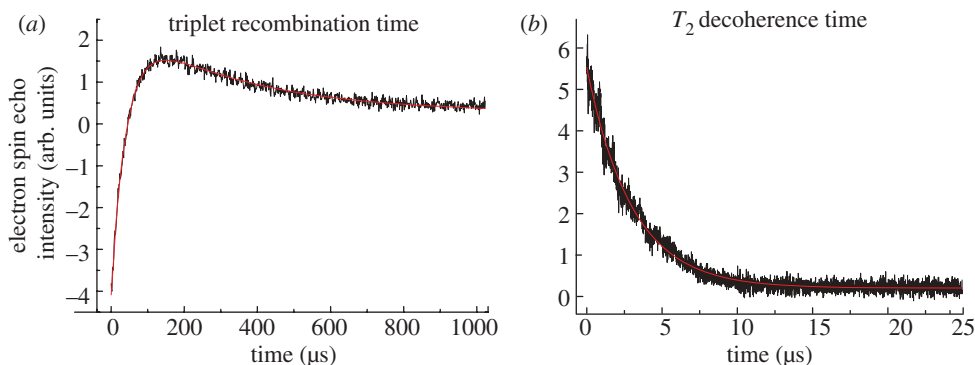


Figure 5. (a) Fitting of the inversion–recovery trace of DMHFP to a biexponential gives a slow decay component of 267 μs and a faster component of 34 μs , attributed to the different relaxation rates of the triplet sublevels back to the ground state (346 mT, 5 K). (b) Measurement of T_2 using a Hahn echo decay at the same field and temperature yields a time of about 3 μs . (Online version in colour.)

the longest of which is 267 μs (figure 5a). By contrast, T_2 at the same field is much shorter and was measured using a Hahn echo sequence to be approximately 3 μs (figure 5b). The field-swept spectrum was found to be temperature independent at temperatures from 5 to 50 K.

For the determination of the hyperfine coupling of the triplet to the ^1H and ^{31}P nuclear spins, we use the Davies ENDOR pulse sequence, and we apply microwave pulses of the same length as in the previous pulsed experiments and 12 μs radiofrequency (RF) pulses. Davies ENDOR spectra at four field positions (*A*, *B*, *C*, *D*, with respect to figure 5) are shown in figure 6a, indicating the nuclear spin resonance frequencies.

For each EPR transition joining two triplet sublevels (i.e. $T_+ \rightarrow T_0$, or $T_0 \rightarrow T_-$), there are two measurable ENDOR resonance frequencies corresponding to the nuclear spin splitting in each sublevel. These frequencies are

$$\omega_{\text{ENDOR}(0)} = \omega_{0,I} \quad \text{and} \quad \omega_{0,I} \pm A_H, \quad (3.1)$$

depending on whether the T_+ or T_- level is involved, where I is the nuclear spin, ω_0 is the Larmor frequency and A_H is the effective hyperfine splitting at a particular magnetic field orientation. In the ENDOR spectra, we observe two intense, narrow lines at $\omega_{0,H} \approx 6$ MHz and $\omega_{0,P} \approx 15$ MHz which correspond to the Larmor frequencies of ^{31}P and ^1H . The weakly resolved peak at around 3.8 MHz is the Larmor frequency of ^{13}C present at low natural abundance in the fullerene cage or as impurities in the solvent.

In figure 6b, we plot separately the two ENDOR spectra at fields *A*, *D*, in order to demonstrate the effect of the RF excitation on the electron spin echo intensity in the ENDOR experiment, to extract the ENDOR efficiency. The high intensity of the Larmor frequency ENDOR peaks corresponds to an ENDOR efficiency of 90–100%. In the ENDOR spectrum at each magnetic field, we also observe two less intense peaks that show a much stronger magnetic field dependence (e.g. at ≈ 17 MHz and ≈ 21 MHz when measured at the *A* field position). These represent the hyperfine splittings in the T_{\pm} subspace, and show substantially lower ENDOR efficiencies. Therefore, for high-fidelity control operations, it is better to use nuclear spin transitions within the T_0 triplet subspace. The magnitude of the hyperfine splitting is directly obtained from the shift of the ENDOR lines compared with the Larmor frequency. The substantial magnetic field dependence of these peaks indicates anisotropic hyperfine interactions, whereas the width of these peaks arises from the presence of a spread of molecular orientations.

The assignment of these two peaks to the nuclear spins can be performed using equation (3.1), which indicates that ENDOR peaks should appear symmetrically around the Larmor frequency. For example, an ENDOR peak appears at about 21 MHz at *A* (338 mT) and at about 9 MHz at *D*

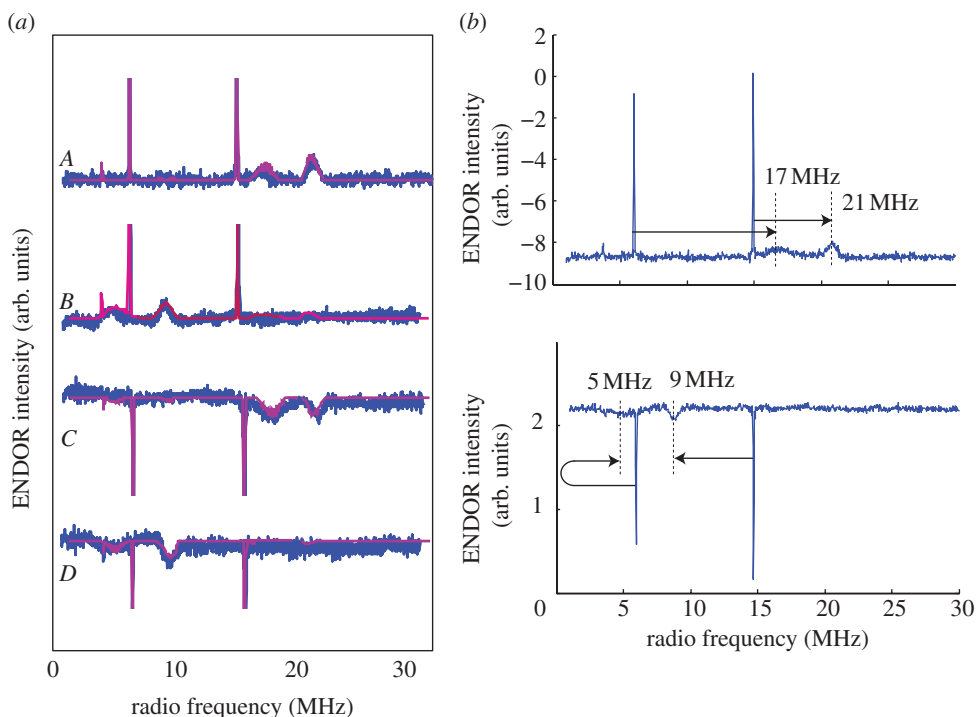


Figure 6. (a) ENDOR spectra of DMHFP measured at four magnetic fields of the ESE-FS spectrum shown in figure 4 (adapted from [17]). The narrow line around 15 MHz is the proton Larmor frequency, whereas the line at around 6 MHz is the Larmor frequency of the phosphorus. The two intense peaks are clipped to better show the weaker resonances. (b) We show the ENDOR spectra at positions A and D to demonstrate the high ENDOR fidelity of the two ENDOR peaks at the Larmor frequency. With the arrows, we mark the frequency shifts from the Larmor peaks for the estimation of the hyperfine interaction. (Online version in colour.)

(358 mT), shifted in each case by about 6 MHz from the ^1H Larmor frequency at 15 MHz. Similarly, hyperfine peaks arising from the ^{31}P appear at about 17 and 5 MHz, shifted by 11 MHz from the Larmor frequency of 6 MHz.

After assigning the hyperfine peaks to each of the two nuclear spins, we move on to simulate the ENDOR spectra and confirm those values. Fitting the ENDOR traces in all four different field lines, we determine the isotropic component hyperfine interaction of the ^1H and ^{31}P to be $A(^1\text{H}) = 5.9$ and $A(^{31}\text{P}) = 11$ MHz. The z-axis of the ZFS tensor coincides with the z-axis of the hyperfine tensor, so no additional orientations were required for fitting the spectra. The hyperfine tensor compares well with DFT studies [17].

Additional investigation of the ENDOR linewidth of the narrow ^1H Larmor frequency line was performed by varying the length of the RF_H pulse. According to the decay shown in figure 5a, there is a maximum window of the order of the recombination time (≈ 250 μs) for the application of an RF pulse. Using an RF π -pulse length of up to 230 μs , an ENDOR linewidth of about 4 kHz was observed (though still mostly limited by the excitation bandwidth of the RF pulse), indicating long nuclear spin T_2 times.

Nuclear spins of molecules have been studied as potential quantum bits, or qubits, the building blocks of quantum computers [21,22]. Spin manipulation (e.g. by (ENDOR) or nuclear magnetic resonance (NMR)) can be used create single-qubit logical operations, whereas couplings between spins can be used for multiple-qubit operations. In order to explore the potential of a molecule to support high-fidelity quantum logic operations, it is necessary to fully characterize the spin Hamiltonian, as well as understand spin dynamics such as relaxation. We have combined X- and Q-band EPR studies to obtain a precise set of spin Hamiltonian parameters for the DMHFP

system. The similarity between the ESE-FS spectrum at X-band (presented in [17]) and the TR-EPR Q-band spectrum (figure 3) reveals (i) the small impact of the T_2 relaxation on the spectrum and (ii) the small g -anisotropy (g_{aniso} ($g_{\text{min}} - g_{\text{max}}$) = 0.00198). From the ESE-FS experiments at X-band (figure 4), the fact that the spectrum remains symmetric as it decays following laser excitation indicates that triplet recombination, rather than spin–lattice relaxation, is the dominant decay mechanism [23]. The large intensity of the ENDOR peak at the Larmor frequency indicates that high-fidelity spin manipulation can be achieved for nuclear spin transitions with no contribution from the hyperfine coupling (i.e. those which lie within the T_0 subspace of the triplet). The above findings indicate that the heteronuclear DMHFP is a molecular system which could be used to implement basic nuclear spin entangling gates, as explored in detail in [17].

4. $\text{H}_2@C_{60}$

(a) Introduction

Recent years have seen an ongoing effort to gain a complete understanding of the properties of small-molecule endofullerenes. In these systems, one or more small molecules such as dihydrogen, H_2 , or water, H_2O , are trapped inside fullerene cages [24,25]. In this section, we present EPR and ENDOR studies on the endohedral system $\text{H}_2@C_{60}$. The synthesis of these fullerenes is achieved by a technique called ‘molecular surgery’. This process involves the chemical creation of a stabilized hole in C_{60} , followed by the application of high temperature and pressure which is increased gradually until the H_2 is inserted in the fullerene. Reduction in the pressure and temperature stabilizes the H_2 inside the fullerene and the ‘surgery’ is completed by chemically closing the hole and regenerating the pristine fullerene cage. A detailed description of these stages is given in [24].

The behaviour of the trapped molecules can be probed by interactions with microwave, infrared [26,27] and RF [28] radiation. According to the Pauli exclusion principle, H_2 can exist in two distinct allotropic forms: the *ortho*- H_2 with nuclear spin 1 and the *para*- H_2 with nuclear spin 0. Ortho-to-para conversion is slow in the absence of a spin catalyst: at low temperature, the *para*- H_2 has the lowest energy and the *ortho*- H_2 is metastable with a lifetime of months. The ortho-to-para ratio is temperature dependent, and it is 3:1 at 300 K and 1:1 at 77 K and 2:1000 at 20 K.

Because the reported time scales required for the *ortho*–*para* ratio to reach equilibrium can be months, it is essential to find an effective spin catalyst in order to induce a fast interconversion between these two forms [29]. Usually an electron or a nuclear spin that creates an effective magnetic field gradient across the positions of the two spins can serve this purpose [30,31]. For example, the *ortho*-to-*para* conversion can be driven by the photochemical formation of an electronic paramagnetic triplet state that is delocalized over the fullerene cage. This idea was put into practice in the work of Frunzi *et al.* [32], who reported the effect of photoexcitation of the fullerene triplet on the (room temperature) NMR spectra of $\text{H}_2@C_{60}$ and $\text{H}_2@C_{70}$. The *ortho*–*para* ratio was recorded before and after optical irradiation at 77 K, and whereas the $\text{H}_2@C_{60}$ signal showed no significant variation of the equilibrium composition at room temperature that of $\text{H}_2@C_{70}$ exhibited a reduction in the *ortho*- H_2 signal which is compatible with the expected 1:1 ratio of the nuclear spin isomers of H_2 at 77 K. The difference in the behaviour of $\text{H}_2@C_{60}$ and $\text{H}_2@C_{70}$ was attributed to the different triplet-state lifetimes of C_{60} and C_{70} .

(b) EPR and ENDOR

In this work, we performed pulsed EPR experiments with laser excitation at 532 nm to study the properties and the dynamics of the photoexcited triplet $\text{H}_2@C_{60}$ at 20 K and identify the

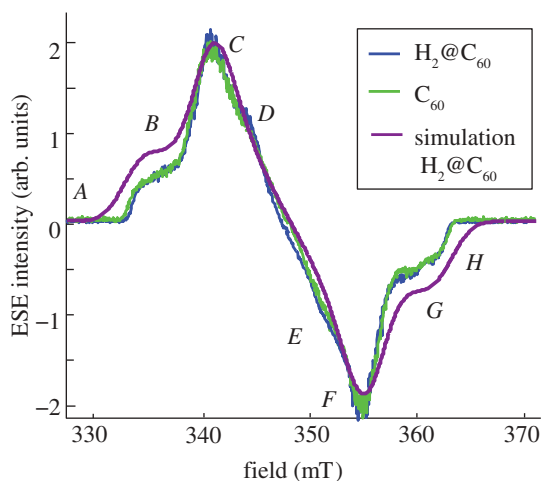


Figure 7. Electron spin echo (ESE)-detected spectrum of the $\text{H}_2@C_{60}$ with fit and pristine C_{60} (X-band, 20 K). For the fitting, we used the ZFS parameters reported in the literature for the triplet C_{60} at the static limit. The spectra have an AAEE pattern which is typical for fullerenes. The labelling of various parts of the spectrum A–H indicates field positions at which ENDOR spectra were taken (figure 8). (Online version in colour.)

interactions of the *ortho*- H_2 spins with the triplet state. It should be noted that the *para*- H_2 does not interact with the triplet state since it has zero spin.

The ESE-FS spectrum of $\text{H}_2@C_{60}$ at 20 K is shown in figure 7 together with the triplet C_{60} spectrum for reference. The pulse lengths were 20 and 40 ns for $\pi/2$ and π pulses, respectively. Both spectra are almost identical and they are polarized in absorption in low fields and in emission in high fields. The resemblance of the two spectra shows the negligible impact of the presence of the H_2 molecule in the line shape of the $\text{H}_2@C_{60}$ spectrum.

For the simulation, we adopt the g -tensor, $g_{xx} = 1.9992$, $g_{yy} = 1.9992$, $g_{zz} = 2.0003$ predicted in [33] by W-band spectroscopy at 1.5 K for C_{60} , whereas the ZFS D and the anisotropy E determined initially by Wasielewski *et al.* [30] are $D = |340|$ MHz and $E = |15|$ MHz. We also adopted a negative D tensor as concluded later on by Heuvel *et al.* which reveals that the T_z sublevel has the highest energy. The population of the triplet sublevels is similar to that observed for the fullerene C_{60} [33–35] and the $|p_x - p_z|/|p_y - p_z|$ population ratio is 1.2.

By taking a closer look at the fitting of the $\text{H}_2@C_{60}$ spectrum, we observe that the outer peaks are not accurately fitted despite using these well-established values. According to the literature the Jahn–Teller distorted triplet C_{60} spectrum is governed by pseudo-rotation effects, thus it cannot be simulated satisfactorily by considering a static model that incorporates Zeeman and ZFS interactions of one triplet state [34]. Pseudo-rotation effects concern the rotation of the magnetic axes (ZFS axes) caused by the conversion of the distorted C_{60} between degenerate states, and affect significantly the shape of the EPR spectrum at different temperatures and delays after the laser pulse. This discrepancy is also observed here for the $\text{H}_2@C_{60}$ and a study of possible pseudo-rotation effects is currently under investigation.

A common characteristic in randomly oriented solutions is that the EPR spectrum lacks resolved hyperfine splittings mainly as a result of the anisotropy of the ZFS and the dipolar hyperfine broadenings. In order to resolve the hyperfine interaction between the triplet and the endohedral nuclear spins, we performed Mims ENDOR experiments at 20 K for $\text{H}_2@C_{60}$, as well as empty C_{60} as a control. Figure 8*a–d* shows ENDOR spectra at two magnetic field positions which correspond to the two innermost peaks of the EPR spectrum (marked C and F on figure 7). For both molecules, a peak at the Larmor frequency for ^1H is observed, where the symmetric splittings are artefacts arising from the RF pulse applied. The existence of this peak for the empty C_{60} samples originates from residual protons in the deuterated-toluene solvent. However, an

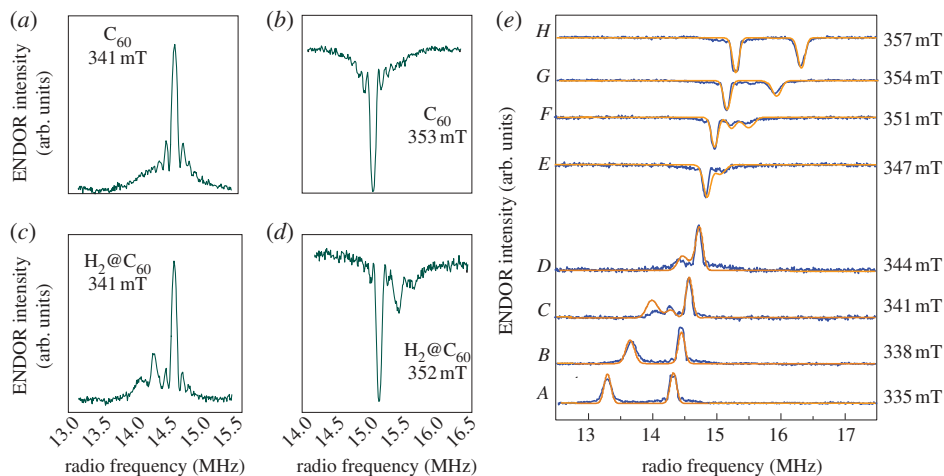


Figure 8. ENDOR spectra of (a,b) empty C_{60} and (c,d) $H_2@C_{60}$ at two field positions C, F , with reference to figure 7. An additional ENDOR peak is seen for $H_2@C_{60}$ on either side of the main Larmor frequency peak, arising from the hyperfine coupling between the triplet and the *ortho*- H_2 . (e) ENDOR spectra at magnetic fields marked $A-H$ in the ESE-detected spectrum. By changing the magnetic field, molecules with different orientations are selected: the shift of the hyperfine interaction peak moves as the magnetic field changes, indicating an anisotropic hyperfine interaction. The slight shift on the main proton line with magnetic field is as expected for the 1H Larmor frequency. Fitting of the eight ENDOR spectra gives principal values of the hyperfine tensor: $A_{xx} = 0.25$, $A_{yy} = 0.75$, $A_{zz} = -1.05$ MHz. (Online version in colour.)

additional ENDOR peak is observed to the left and right of the Larmor frequency line in the case of $H_2@C_{60}$ (figure 8c–d), which arises from the hyperfine splitting of the H_2 *ortho*-state, in the T_{\pm} subspaces of the fullerene triplet.

Further H_2 ENDOR spectra were recorded at different magnetic fields ($A-H$, with respect to figure 7) in order to extract the hyperfine coupling tensor (figure 8e). The magnetic field dependence of the peak arising from the hyperfine splitting indicates an anisotropic hyperfine tensor, whereas the slight frequency shift of the main Larmor frequency peak is as expected according to the 1H nuclear spin gyromagnetic ratio. As expected, the hyperfine peaks appear symmetrically around the Larmor frequency at different sides of the EPR spectra, and from the ENDOR spectra taken at fields A and H we can determine that the $|A_{zz}|$ component of the hyperfine interaction is ≈ 1 MHz. Fitting the ENDOR traces for all different magnetic fields, we determine the hyperfine tensor of the $H_2@C_{60}$ to be $A_{xx} = 0.25$, $A_{yy} = 0.75$, $A_{zz} = -1.05$ MHz (figure 8f). As the z -axis of the ZFS tensor coincides with the z -axis of the hyperfine tensor no additional orientations were required for fitting of the spectra. As we observe *ortho*- H_2 in the ENDOR spectra at this temperature (20 K), we can infer that negligible *ortho*-to-*para* conversion has occurred for $H_2@C_{60}$, consistent with the result of [32]. The hyperfine tensor is calculated in the following section using DFT and reveals a very good agreement with the experimental values.

After extracting the hyperfine tensor, we measure the *ortho*- H_2 spin decoherence time by applying the pulse sequence shown in figure 9a. The sequence is based on Mims ENDOR with the difference that the RF π pulse is now replaced with a nuclear spin Hahn echo pulse sequence whose delay time τ_n is swept. We use a fixed time window of 320 μs to remove any effect of the triplet relaxation and we perform Rabi oscillations to manipulate coherently the nuclear spin by increasing gradually the length of the RF pulse and calibrate the measurement of nuclear spin coherence through electron spin echo intensity. For clarity, we also present the upper and lower levels of electron spin echo intensity arising from the absence and presence of the RF π pulse, using the same fixed time interval. The decay of the nuclear spin coherence was fitted to an exponential with $T_2 = 440$ μs (figure 9b,c).

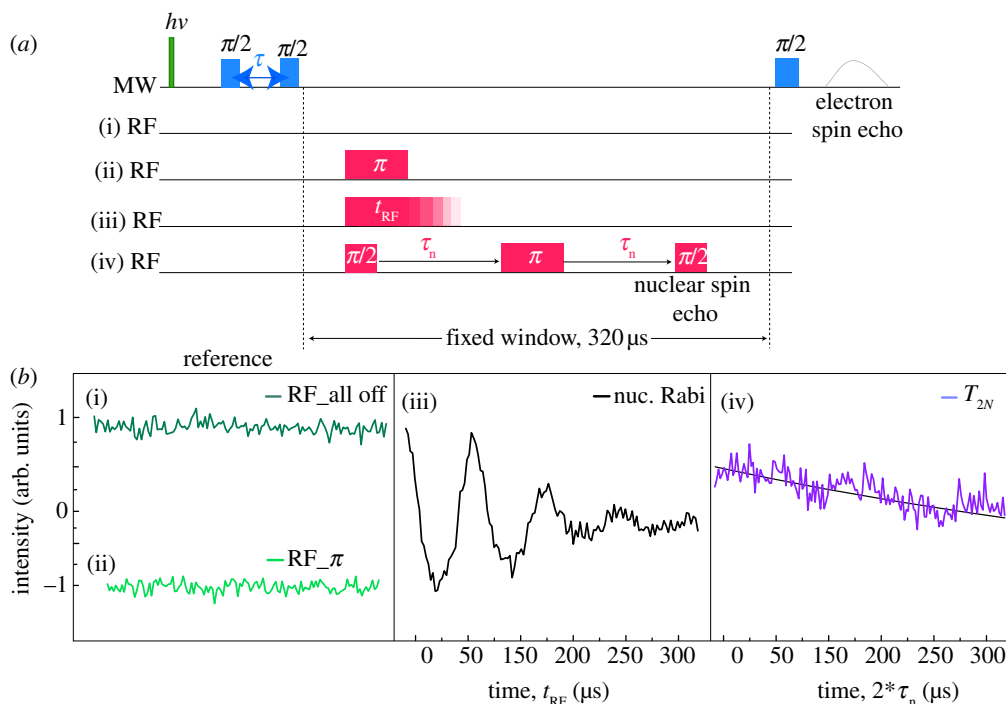


Figure 9. Pulse sequences (a) and experimental traces (b) based on the Mims ENDOR sequence, applied to $\text{H}_2@C_{60}$. Reference traces for (i) absence and (ii) presence of an RF π pulse are used to normalize subsequent measurements on nuclear spin coherence. (iii) Nuclear spin Rabi oscillations are detected by monitoring the electron spin echo intensity while varying the length of a single RF pulse up to a maximum of 320 μs . The first minimum of the Rabi oscillations represents the application of an RF π pulse. (iv) The *ortho*-H₂ nuclear spin T_2 , in the presence of the fullerene triplet. At the point of the formation of the nuclear spin echo, an RF $\pi/2$ pulse transfers the nuclear spin coherence to a nuclear spin polarization, which is then measured by the electron spin echo intensity. Fitting the observed decay to a single exponential function, we extract a T_2 of 440 μs . (Online version in colour.)

5. Density functional theory calculations of the hyperfine interaction

First-principles electronic-structure calculations are capable of predicting the parameters related to EPR and NMR spectroscopy [36–39]. Among these, those based on DFT offer the best scaling properties with respect to the increase in computational cost and resource usage. Hence, they are particularly suited to the purpose sought herein, because we are seeking to model molecules made of 60 carbon atoms.

Furthermore, modelling the system dealt with herein poses two major problems, i.e. the quantum motion of H₂ within C₆₀ and the weak interaction between them. In fact, an unsatisfactory performance of DFT is often observed when dealing with molecules (or parts thereof) that interact through weak dispersive forces. This issue is particularly sensitive here, because the H₂ molecule is embedded within C₆₀ (in whatever electronic state) but does not form any covalent bond with it; indeed, it precisely interacts with the interior of the C₆₀ cage via dispersion. Therefore, all issues that involve an estimation of the energetics of H₂/C₆₀ interaction must face this problem. However, some modern density functionals (or modifications thereof) take dispersion into account; in this work, we have adopted a correction scheme proposed by Grimme *et al.* [40] to the BP86 functional.

Second, modelling H₂ encapsulated in C₆₀ may be hindered by the quantum nature of its internal dynamics [41]. Even though a full description of the quantum roto-translational (RT) energy levels is available, that approach does not provide the electronic structure of the H₂@C₆₀ ensemble, required for predicting EPR parameters. Such calculations can be currently carried out

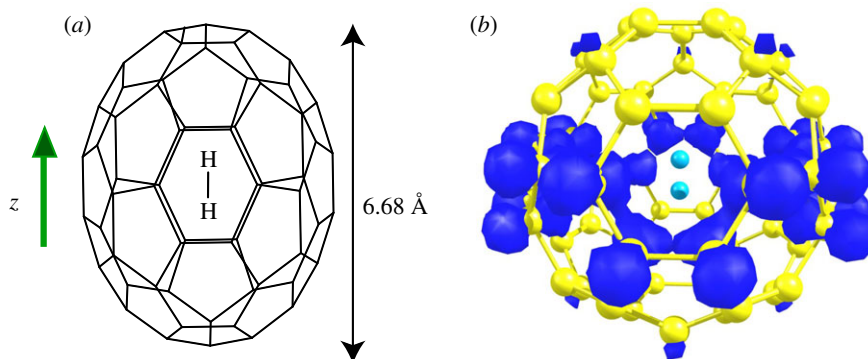


Figure 10. (a) Representation of the elongation of the $\text{H}_2@C_{60}$ along the z -axis in the triplet state. The average distance between centres of pentagonal faces (greatly exaggerated for clarity) is estimated at around 6.68 Å. (b) The spin density follows a belt perpendicular to the long axis of the fullerene. (Online version in colour.)

only on fixed geometrical arrangements which treat RT motion classically. As mentioned above, this approach is questionable for $\text{H}_2@C_{60}$. Nevertheless, in a related work in this Theo Murphy Meeting Issue [42], we have demonstrated that, at least at room temperature, the error involved in treating the motion of H_2 classically is negligible.

A final issue concerns the open-shell nature of the species. While the calculation of NMR properties of closed-shell, diamagnetic molecules is now widely used to aid structure determination [36–39,43], the corresponding computations for open-shell, paramagnetic species are comparatively less developed. Nevertheless, it has been shown that DFT methods can be used to predict NMR and EPR parameters for a variety of paramagnetic organic, organometallic and inorganic molecules [44–56].

In order to gain an atomic-level understanding of the endohedral $\text{H}_2@C_{60}$, determine the position of the H_2 in the fullerene cage and extract the principal axis of the hyperfine tensor, we perform DFT calculations and we compare results with experimental values.

(a) Computational details

Density functional calculations were carried out with the ADF 2012 suite of programs [57] with the PBE0 [58] hybrid exchange–correlation functional. Dispersion energies were modelled via Grimme’s D3 correction [40]. Triple-zeta basis sets made up of Slater functions with one (TZP) or two (TZ2P) sets of polarization functions were used for geometry optimization and properties, respectively. All calculations of triplet states were spin-unrestricted and run without symmetry (even though some arrangements have high symmetries), in order to ensure maximum flexibility and to avoid spurious constraints. Hyperfine couplings (A tensors) were computed at the optimized geometry with the PBE0-D3/TZ2P method.

(b) Density functional theory results

As a first approach to the electronic structure of singlet and triplet $\text{H}_2@C_{60}$, the H_2 molecule was placed at the centre of the C_{60} cage, with the H–H axis aligned along a direction connecting two pentagonal faces (z -axis). Geometry optimization of the singlet state showed that $\text{H}_2@C_{60}$ preserves its spherical shape, while an elongation along the z -axis is observed in the triplet state (figure 10a). This picture is quite similar to what is observed for empty C_{60} in the triplet state where Jahn–Teller effects distort the cage. The spin density is distributed around the fullerene belt (figure 10b). In order to determine the average position of the H_2 in the fullerene cage, we calculated the energetics of the displacement of H_2 along x in the singlet and triplet states and along z in the triplet state (figure 11a). The plot of the energy of the structures in relation to

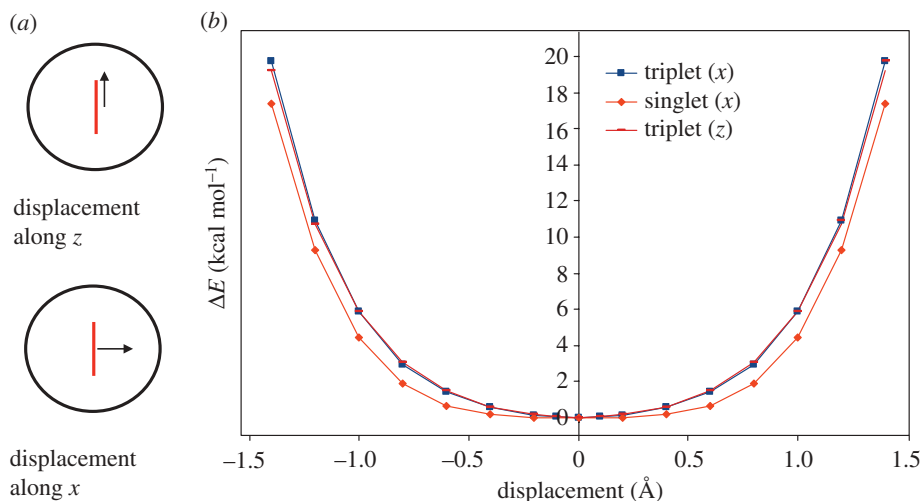


Figure 11. (a) Schematic of the displacement of the H_2 along the z - and x -axis, respectively. The position of the H_2 is marked with a vertical line. (b) Plot of the energy of the $\text{H}_2@C_{60}$ in the singlet and triplet states with the displacement along x and z , respectively. The most stable structures in all configurations are those with the H_2 placed at the centre of the fullerene cage. (Online version in colour.)

the displacement is shown in figure 11b, which reveals that the most stable structures place the H_2 in the centre of the fullerene cage. The energy minimum (at the centre) is somewhat more pronounced for triplet than for singlet C_{60} ; however, the direction of displacement is irrelevant. Small displacements (up to 0.6 Å) raise the energy by approximately 1.5 kcal mol⁻¹.

Therefore, for practical purposes, one can assume that on average the encapsulated hydrogen molecule resides at the centre of C_{60} . However, because the symmetry (and hence the spin density) of triplet C_{60} and $\text{H}_2@C_{60}$ is lower than in the singlet, it becomes interesting to probe into the effect caused by different H_2 orientations within the cage, which seem energetically reachable as shown above.

Thus, we carried out further calculations with the H_2 molecule initially arranged along the x - and y -axes, as well as the axes defined by the bisector of the xy , xz and yz planes in the positive and negative directions ($\pm xy$, $\pm xz$ and $\pm yz$ axes for short), for a total of nine orientations. Each calculation was run independently with the methods described above, and afforded energy, structure and hyperfine coupling.

Geometry optimization resulted in a H–H distance of 0.758 Å in all orientations, which is identical to the value for the singlet state. This distance is slightly longer than that calculated for H_2 at the same level of theory (0.746 Å) or the experimental value (0.740 Å). Therefore, encapsulation into C_{60} (whether in the singlet or triplet state) results in an elongation of the H–H bond by approximately 0.1 Å. This finding may be relevant in connection with the rate of *ortho*–*para* conversion, which was shown to depend on that distance [59]. Concerning the arrangement of encapsulated H_2 , geometry optimization invariably led to no change in its orientation with respect to the original one, indicating that the forces acting on the whole molecule are extremely small. This is consistent with a weak interaction between H_2 and C_{60} ; however, we did not compute absolute interaction energies. All orientations have relative energies within 0.1 kcal mol⁻¹ (z being most stable), which is smaller than the known accuracy of DFT methods; hence, all orientations can be considered energetically equivalent and equally populated.

The principal values of the hyperfine tensor which is axially symmetric are $A_{xx} = 0.78$, $A_{yy} = 0.78$, $A_{zz} = -1.2$ MHz for all orientations, whereas the isotropic value A_{iso} is 0.12 MHz. The calculated hyperfine tensor agrees well with the experiment.

Because the spin density is distributed across the belt as shown in figure 10b, one would not expect constant values of A for all arrangements of H_2 inside. This is understood by examining

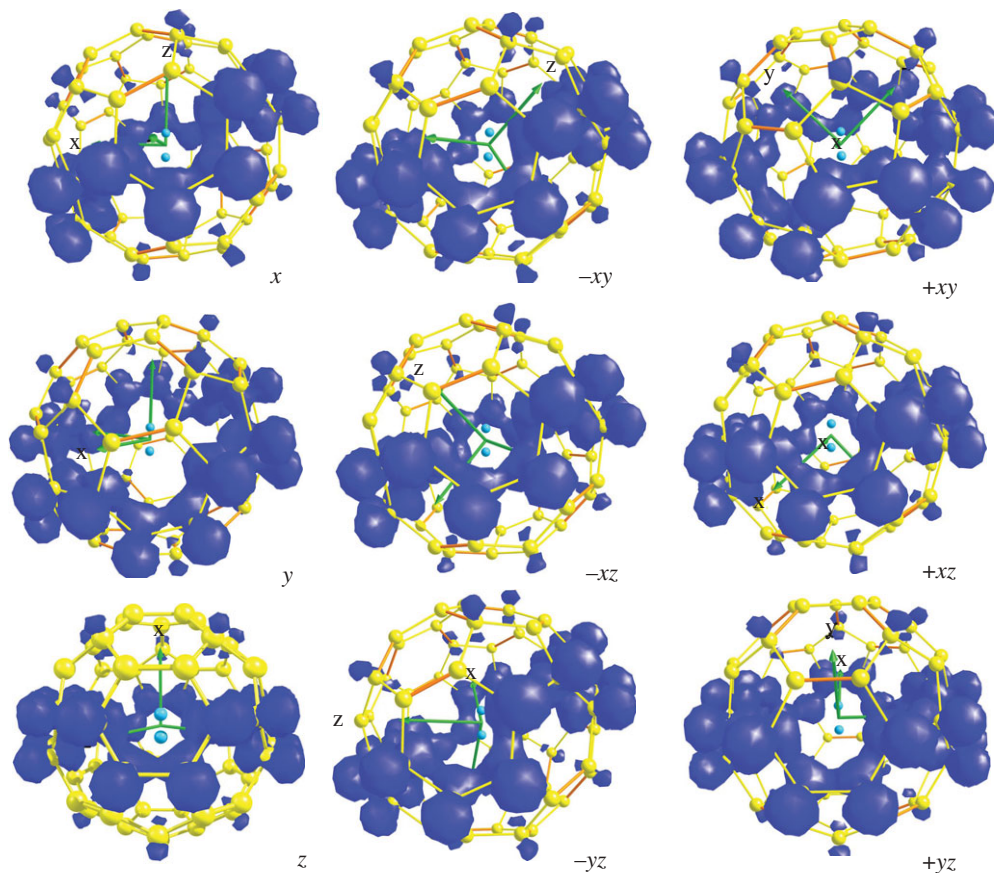


Figure 12. Spin densities of the triplet state of the $\text{H}_2@C_{60}$. The H_2 is always oriented vertically for clarity, whereas the axes are rotated. The elongated axes is always perpendicular to the belt plane. (Online version in colour.)

the electronic structure of all orientations investigated (figure 12); contrary to expectation, the spin density is found to be quite mobile and is always located at the closest belt perpendicular to the H_2 axis, so that the hydrogen nuclear spins experience a very similar density regardless of its orientation.

6. Conclusions

Photoexcitation of fullerenes and their derivatives can generate a hyperpolarized triplet state lasting for several hundreds of microseconds, allowing these systems to be probed by EPR and ENDOR spectroscopy for the study of dynamics and couplings between nuclear spins located within, or bonded to, the fullerene cage. We present characterization studies of the DMHFP molecule and discuss how the nuclear spins attached to the cage can be hyperpolarized and detected via the electron spin triplet state. We applied similar methodology to study endohedral $\text{H}_2@C_{60}$ and we extract the hyperfine tensor for coupling to endohedral *ortho*- H_2 . No appreciable *ortho*-to-*para* conversion was observed during the ENDOR experiments at 20 K for the $\text{H}_2@C_{60}$ molecule.

Understanding the interactions between the *ortho*-hydrogen and the electronic triplet state in $\text{H}_2@$ -fullerenes provides an important step in the design of systems where the *para*-*ortho* conversion can be controlled with the aim of inducing large polarization in the nuclear spins. Future experiments will extend these studies to other small-molecule endohedral fullerenes, such as $\text{H}_2@C_{70}$, in which the fullerene triplet state was found to catalyse *ortho*-*para* conversion [32].

Acknowledgements. This research is supported by the EPSRC through the Materials World Network (EP/I035536/1), CAESR (EP/D048559/1) and a Basic Technology Grant ‘Molecular Spintronics’ (EP/F041349/1), as well as by the European Research Council under the European Community’s Seventh Framework Programme (FP7/2007-2013)/ERC grant agreement no. 279781. J.J.L.M. is supported by the Royal Society. EPR and ENDOR experiments were performed in CAESR, University of Oxford, and at University College London. Financial support from the University of Padova (PRAT CPDA103095) is gratefully acknowledged. Calculations were run on the LINUX cluster of the Laboratorio Interdipartimentale di Chimica Computazionale (LICC) of the University of Padova.

References

1. McGlynn SP, Azumi T, Kinoshita M. 1969 *Molecular spectroscopy of the triplet state*, pp. 329–402. International Series in Chemistry. Englewood Cliffs, NJ: Prentice-Hall.
2. Hirota N, Yamauchi S. 2003 Short-lived excited triplet states studied by time resolved EPR spectroscopy. *J. Photochem. Photobiol. C Photochem. Rev.* **4** 109–124. (doi:10.1016/S1389-5567(03)00024-8)
3. Di Valentin M, Kay CWM, Giacometti G, Möbius K. 1996 A time-resolved electron nuclear double resonance study of the photoexcited triplet state of P680 in isolated reaction centers of photosystem II. *Chem. Phys. Lett.* **248**, 434–441. (doi:10.1016/0009-2614(95)01347-4)
4. Dinse KP, Winscom CJ. 1982 Optically detected ENDOR spectroscopy. In *Triplet state ODMR spectroscopy: techniques and applications to biophysical systems* (ed. RH Clarke), pp. 83–136. New York, NY: John Wiley & Sons.
5. Haarer D, Wolf HC. 1970 ESR studies on triplet excitons in anthracene and naphthalene monocrystals. *Mol. Cryst. Liq. Cryst.* **10**, 359–380.
6. Hutchison JCA, Magnum BW. 1958 Paramagnetic resonance absorption in naphthalene in its phosphorescent state *J. Chem. Phys.* **29**, 952–953. (doi:10.1063/1.1744621)
7. Philips D. 1995 The photochemistry of sensitizers for photodynamic therapy. *Pure Appl. Chem.* **67**, 117–126. (doi:10.1351/pac199567010117)
8. Geacintov NE, Brenner HC. 1989 The triplet state as a probe of dynamics and structure in biological macromolecules. *Photochem. Photobiol.* **50**, 841–858. (doi:10.1111/j.1751-1097.1989.tb02916.x)
9. Salikhov KM, Molin YN, Sagdeev RZ, Buchachenko AL. 1984 *Magnetic and spin effects in chemical reactions*. Amsterdam, The Netherlands: Elsevier.
10. Lubitz W, Lendzian F, Bittl R. 2002 Radicals, radical pairs and triplet states in photosynthesis. *Acc. Chem. Res.* **35**, 313–320. (doi:10.1021/ar000084g)
11. Clarke RH. 1982 *Triplet state ODMR spectroscopy: techniques and applications to biophysical systems*. New York, NY: John Wiley & Sons.
12. Bachert P, Brunner H, Hausser KH, Colpa JP. 1984 Microwave-induced optical nuclear polarization (MIONP) of benzophenone in dibromodiphenylether *Chem. Phys.* **91**, 435–447. (doi:10.1016/0301-0104(84)80076-2)
13. Takeda K, Takegoshi K, Terao T. 2004 Dynamic nuclear polarization by electron spins in the photoexcited triplet state. I. Attainment of proton polarization of 0.7 at 105 K in naphthalene *J. Phys. Soc. Jpn.* **73**, 2313–2318. (doi:10.1143/JPSJ.73.2319)
14. Schmidt J, van den Heuvel DJ, Henstra A, Lin T-S, Wenckebach W. Nuclear spin orientation via pulsed EPR and optically cooled triplet electron spins. *Pure Appl. Chem.* **64**, 859. (doi:10.1016/0009-2614(92)90008-B)
15. Akhtar W, Filidou V, Sekiguchi T, Kawakami E, Itahashi T, Vlasenko L, Morton JJJ, Itoh KM. 2012 Coherent storage of photoexcited triplet states using ²⁹Si nuclear spins in silicon. *Phys. Rev. Lett.* **108**, 097601. (doi:10.1103/PhysRevLett.108.097601)
16. Schaffry M *et al.* 2012 Entangling remote nuclear spins in chromophores. *Phys. Rev. Lett.* **104**, 200501. (doi:10.1103/PhysRevLett.104.200501)
17. Filidou V, Simmons S, Karlen SD, Giustino F, Anderson HL, Morton JJJ. 2012 Ultrafast entangling gates between nuclear spins using photo-excited triplet states. *Nat. Phys.* **8**, 596–600. (doi:10.1038/nphys2353)
18. Isobe H, Chen A-J, Solin N, Nakamura E. 2005 Synthesis of hydrophosphorylated fullerene under neutral conditions. *Org. Lett.* **7**, 5633–5635. (doi:10.1021/ol0522586)
19. Brustolon M, Giamello E. 2009 *Electron paramagnetic resonance: a practitioners toolkit*. London, UK: John Wiley & Sons.

20. Stoll S, Schweiger A. 2006 EasySpin, a comprehensive software package for spectral simulation and analysis in EPR. *J. Magn. Reson.* **178**, 42–55. (doi:10.1016/j.jmr.2005.08.013)
21. Cory DG, Fahmy AF, Havel TF. 1997 Ensemble quantum computing by NMR spectroscopy. *Proc. Natl Acad. Sci. USA* **94**, 1634–1639. (doi:10.1073/pnas.94.5.1634)
22. Gernhenfeld NA, Chuang IL. 1997 Bulk spin-resonance quantum computation. *Science* **275**, 350–356. (doi:10.1126/science.275.5298.350)
23. Dauw XLR, Poluektov OG, Warntjes JBM, Bronsveld MV, Groenen EJJ. 1998 Triplet-state dynamics of C₇₀. *J. Phys. Chem. A*. **102**, 3078–3082. (doi:10.1021/jp980925p)
24. Komatsu K, Murata M, Murata Y. 2005 Encapsulation of molecular hydrogen in fullerene C₆₀ by organic synthesis. *Science* **307**, 238–240. (doi:10.1126/science.1106185)
25. Kurotobi K, Murata Y. 2011 A single molecule of water encapsulated in fullerene C₆₀. *Science* **333**, 613–616. (doi:10.1126/science.1206376)
26. Mamone S *et al.* 2009 Rotor in a cage: infrared spectroscopy of an endohedral hydrogen–fullerene complex. *J. Chem. Phys.* **130**, 081103. (doi:10.1063/1.3080163)
27. Ge M *et al.* 2011 Infrared spectroscopy of endohedral HD and D₂ in C₆₀. *J. Chem. Phys.* **135**, 114511. (doi:10.1063/1.3637948)
28. Carravetta M *et al.* 2007 Solid-state NMR of endohedral hydrogen–fullerene complexes. *Phys. Chem. Chem. Phys.* **9**, 4879–4894. (doi:10.1039/b707075f)
29. Turro NJ *et al.* 2009 The spin chemistry and magnetic resonance of H₂@C₆₀. From the Pauli principle to trapping a long lived nuclear excited spin state inside a Buckyball. *Acc. Chem. Res.* **43**, 335–345. (doi:10.1021/ar900223d)
30. Wasielewski MR, Neil KRO, Lykke KR, Pellin MJ, Gruen DM. 1991 Triplet states of fullerenes C₆₀ and C₇₀. Electron paramagnetic resonance spectra, photophysics, and electronic structures. *J. Am. Chem. Soc.* **113**, 2774–2776. (doi:10.1021/ja00007a074)
31. Abrogast JW, Darmanyan AP, Foote CS, Diederich FN, Rubin Y, Alvarez MM, Anz SJ, Whetten RL. 1991 Photophysical properties of C₆₀. *J. Phys. Chem.* **95**, 11–12. (doi:10.1002/chin.199113009)
32. Frunzi M *et al.* 2011 A photochemical on–off switch for tuning the equilibrium mixture of H₂ nuclear spin isomers as a function of temperature. *J. Am. Chem. Soc.* **133**, 14 232–14 235. (doi:10.1021/ja206383n)
33. Dauw XLR, van den Berg GJB, van den Heuvel DJ, Poluektov OG, Groenen EJJ. 2000 The triplet wave function of C₆₀ from W-band electron nuclear double resonance spectroscopy. *J. Chem. Phys.* **112**, 7102–7110. (doi:10.1063/1.481305)
34. Bennati M, Grupp A, Mehring M. 1995 Electron paramagnetic resonance lineshape analysis of the photoexcited triplet state of C₆₀ in frozen solution. Exchange narrowing and dynamic Jahn–Teller effect. *J. Chem. Phys.* **102**, 9457–9464. (doi:10.1063/1.468814)
35. Regev A, Gamliel D, Meiklyar V, Michaeli S, Levanon H. 1993 Dynamics of ³C₆₀ probed by electron paramagnetic resonance. Motional analysis in isotropic and liquid crystalline matrices. *J. Phys. Chem* **97**, 3671–3679. (doi:10.1021/j100117a007)
36. Kaupp M, Bühl M, Malkin VG. (eds) 2004 *Calculation of NMR and EPR parameters*. Weinheim, Germany: Wiley-VCH.
37. Mennucci B. 2010 The simulation of UV-Vis spectroscopy with computational methods. In *Computational spectroscopy: methods, experiments and applications* (ed. J Grunenberg), pp. 151–171. Weinheim, Germany: Wiley-VCH.
38. Cimino P, Neese F, Barone V. 2010 Calculation of magnetic tensors and EPR spectra for free radicals in different environments. In *Computational spectroscopy: methods, experiments and applications* (ed. J Grunenberg), pp. 63–104. Weinheim, Germany: Wiley-VCH.
39. Alkorta I, Elguero J. 2010 Computational NMR spectroscopy. In *Computational spectroscopy: methods, experiments and applications* (ed. J Grunenberg), pp. 37–61. Weinheim, Germany: Wiley-VCH.
40. Grimme S, Anthony J, Ehrlich S, Krieg H. 2010 A consistent and accurate ab initio parametrization of density functional dispersion correction (DFT-D) for the elements H–Pu. *J. Chem. Phys.* **132**, 154 104–154 122. (doi:10.1063/1.3382344)
41. Xu M, Sebastianelli F, Bacic Z, Lawler R, Turro NJ. 2008 H₂, HD, and D₂ inside C₆₀: coupled translation–rotation eigenstates of the endohedral molecules from quantum five-dimensional calculations. *J. Chem. Phys.* **129**, 064313. (doi:10.1063/1.2967858)
42. Rastrelli F, Frezzato D, Lawler RG, Li Y, Turro NJ, Bagno A. 2013 Predicting the paramagnet-enhanced NMR relaxation of H₂ encapsulated in endofullerene nitroxides by density-functional theory calculations. *Phil. Trans. R. Soc. A* **371**, 20110634. (doi:10.1098/rsta.2011.0634)

43. Bagno A, Saielli G. 2007 Computational NMR spectroscopy: reversing the information flow. *Theor. Chem. Acc.* **117**, 603–619. (doi:10.1007/s00214-006-0196-z)
44. Moon S, Patchkovskii S. 2004 First-principles calculations of paramagnetic NMR shifts. In *Calculation of NMR and EPR parameters* (eds M Kaupp, M Bühl, VG Malkin), pp. 325–338. Weinheim, Germany: Wiley-VCH.
45. Arbuznikov AV, Vaara J, Kaupp M. 2004 Relativistic spin–orbit effects on hyperfine coupling tensors by density-functional theory. *J. Chem. Phys.* **120**, 2127–2139. (doi:10.1063/1.1636720).
46. Yazyev OV, Helm L, Malkin VG, Malkina OL. 2005 Quantum chemical investigation of hyperfine coupling constants on first coordination sphere water molecule of gadolinium(III) aqua complexes. *J. Phys. Chem. A* **109**, 10 997–11 005. (doi:10.1021/jp053825+)
47. Hrobárik P, Reviakine R, Arbuznikov AV, Malkina OL, Malkin VG, Köhler FH, Kaupp M. 2007 Density functional calculations of NMR shielding tensors for paramagnetic systems with arbitrary spin multiplicity: validation on 3d metallocenes. *J. Chem. Phys.* **126**, 024107. (doi:10.1063/1.2423003)
48. Rastrelli F, Bagno A. 2009 Predicting the NMR spectra of paramagnetic molecules by DFT. Application to organic free radicals and transition-metal complexes. *Chem. Eur. J.* **15**, 7990–8007. (doi:10.1002/chem.200802443)
49. Rastrelli F, Bagno A. 2010 Predicting the H and C NMR spectra of paramagnetic Ru(III) complexes by DFT. *Magn. Reson. Chem.* **48**, S132–S141. (doi:10.1002/mrc.2666)
50. Barone V, Cimino P, Stendardo E. 2008 Development and validation of the B3LYP/N07D computational model for structural parameter and magnetic tensors of large free radicals. *J. Chem. Theor. Comp.* **4**, 751–764. (doi:10.1021/ct800034c)
51. Neese F. 2009 Prediction of molecular properties and molecular spectroscopy with density functional theory: from fundamental theory to exchange-coupling. *Coord. Chem. Rev.* **253**, 526–563. (doi:10.1016/j.ccr.2008.05.014)
52. Autschbach J, Pritchard B. 2011 Calculation of molecular g-tensors using the zeroth-order regular approximation and density functional theory: expectation value versus linear response approaches. *Theor. Chem. Acc.* **129**, 453–466. (doi:10.1007/s00214-010-0880-x)
53. Autschbach J, Patchkovskii S, Pritchard B. 2011 Calculation of hyperfine tensors and paramagnetic NMR shifts using the relativistic zeroth-order regular approximation and density functional theory. *J. Chem. Theor. Comp.* **7**, 2175–2188. (doi:10.1021/ct200143w)
54. Rinkevicius Z, Vaara J, Telyatnyk L, Vahtras O. 2003 Calculations of nuclear magnetic shielding in paramagnetic molecules. *J. Chem. Phys.* **118**, 2550–2561. (doi:10.1063/1.1535904)
55. Pennanen TO, Vaara J. 2005 Density-functional calculations of relativistic spin–orbit effects on nuclear magnetic shielding in paramagnetic molecules. *J. Chem. Phys.* **123**, 174102. (doi:10.1063/1.2079947)
56. Pennanen TO, Vaara J. 2008 Nuclear magnetic resonance chemical shift in an arbitrary electronic spin state. *Phys. Rev. Lett.* **100**, 133002. (doi:10.1103/PhysRevLett.100.133002)
57. te Velde G *et al.* 2001 Chemistry with ADF. *J. Comput. Chem.* **22**, 931–967. (doi:10.1002/jcc.1056)
58. Adamo C, Barone V. 1999 Toward reliable density functional methods without adjustable parameters: the PBE0 model. *J. Chem. Phys.* **110**, 6158–6170. (doi:10.1063/1.478522)
59. Limbach HH, Buntkowsky G, Matthes J, Gründemann S, Pery T, Walaszek B, Chaudret B. 2006 Novel insights into the mechanism of the *ortho/para* spin conversion of hydrogen pairs: implications for catalysis and interstellar water. *Chem. Phys. Chem.* **7**, 551–554. (doi:10.1002/cphc.200500559)